

Nanocrystals growth control during laser anneal of Sn:(α -Si) composites

V. Neimash¹, P. Shepelyavyi², G. Dovbeshko¹, A.O. Goushcha^{1,a),b)}, M. Isaiev³, V. Melnyk¹,
O. Didukh³, A. Kuzmich³

¹Institute of Physics, Nat. Acad. of Sci. of Ukraine, 46, Nauky Pr., Kyiv, Ukraine, 03028

²Institute of Semiconductor Physics, Nat. Acad. of Sci. Ukraine, 45, Nauky Pr., Kyiv, Ukraine, 03028

³ Faculty of Physics, Taras Shevchenko National University of Kyiv, 64/13, Volodymyrska Str., Kyiv, Ukraine, 01601

^{a)}Present address: 21 Nopalitos Way, Aliso Viejo, CA92656, USA

^{b)} Authors to whom correspondence should be addressed. E-mail:goushcha@cox.net

Abstract

An efficient technique for low temperature metal-induced nanocrystalline silicon fabrication is presented. The technique is based on laser anneal of thin films of “amorphous silicon – tin” composites combined with in-situ control with Raman technique. The laser anneal was shown to provide the possibility of fine tuning of nanocrystals size and concentration, which is important in photovoltaic and thermoelectric devices fabrication.

Keywords:

Silicon, Thin films, Nanocrystals, Tin, Metal induced crystallization, Solar cell

1. Introduction

Thin composite films “Si nanocrystals in an amorphous Si matrix” are considered as a promising material for the next-generation solar cells (SC) utilizing quantum dots [1]. This is because the composites possess a unique set of physical properties: direct band-gap mechanism of light absorption, band gap dependence of the nanocrystals size, suppressed Staebler-Vronsky effect, and suitability for fabrication using flexible substrates.

Using of silicon nanocomposites allows to fundamentally increase SC efficiency by creating polymorphic cascade type heterostructures [2,3] and to reduce SC production cost through

advantages of thin films roll-to-roll manufacturing technologies [4,5]. Among the main problems that hinder practical implementation of the advantages of Si nanocrystals (nc-Si) is inadequate control of the size and concentration of Si nanocrystals at economically justified rates of films formation. Therefore, despite a large number of existing technologies of nc-Si production, much attention is still paid to their improvement and finding new alternatives [6-12].

Metal induced crystallization (MIC) of amorphous silicon (α -Si) [13-17] is one of the most promising ways in this field. In particular, tin (Sn) stimulated formation of Si nanocrystals with sizes of 2-5 nm in amorphous Si matrix at temperatures below 450 °C was recently demonstrated [18-20]. The partial volume of the nanocrystall phase of up to 80% was formed. Those experimental results were interpreted using new MIC mechanism proposed in [20,21], which was markedly different from the known mechanisms suggested for other metals [13,15-17]. According to this mechanism, silicon nanocrystals are formed during cyclic processes of formation and disintegration of a supersaturated solution of silicon in Sn. The crystallization occurs in a narrow eutectic layer at the α -Si/Sn interface. In the current paper, we show that the process of Sn-induced crystallization can be initiated and sustained by laser light at relatively low power. We demonstrate that the Raman technique allows monitoring the sample temperature and to simultaneously controlling the nanocrystals' size and partial volume of the nanocrystalline phase by changing the intensity and duration of the laser radiation.

2. Materials and Methods

The samples for studies (see Fig. 1) were made by spot (76x76 mm²) deposition of the electronics-grade silicon and tin (99.92 %) using thermal evaporation in vacuum on the borosilicate glass or Si monocrystalline wafer substrate. Temperature of the substrate was kept near 150 °C during the deposition. The sandwich-type structures were formed by turned deposition of (i) a-Si layer with the thickness Z, (ii) tin layer with the thickness Y, and (iii) a-Si layer with the thickness X.

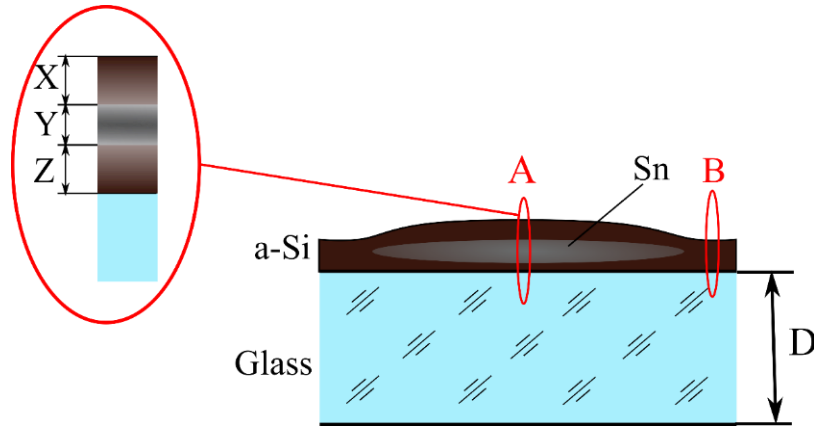
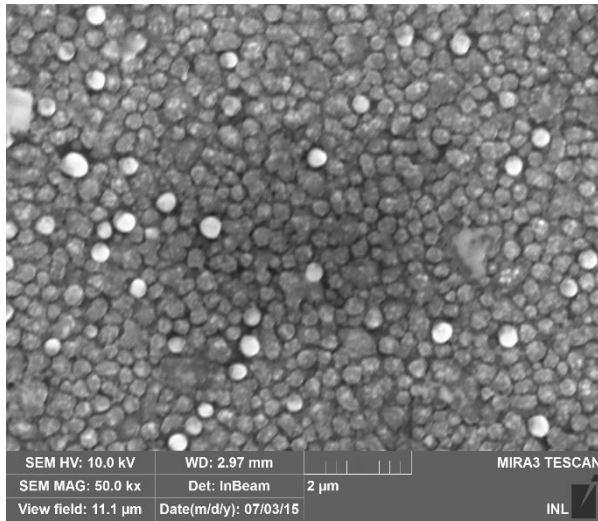


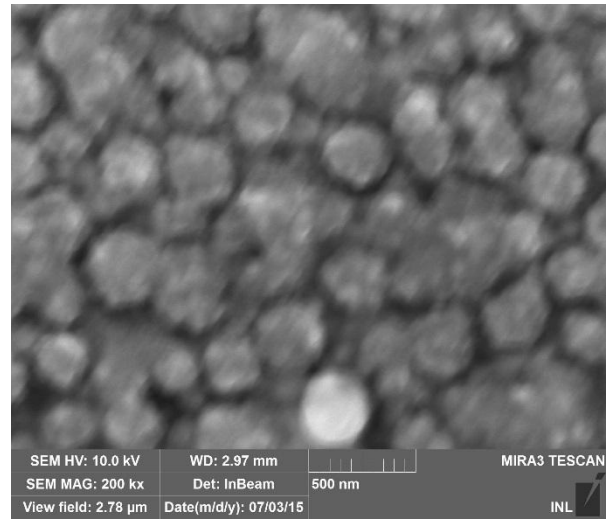
Figure 1. Cross-sectional schematics of the layered structures Si-Sn-Si. “A” and “B” are the two regions of the samples selectively studied in this work.

The values of the layers thickness (X, Y, Z) were varied within the diapason from 50 to 200 nm with the step of 50 nm. All layers were deposited in the same vacuum chamber (10^{-3} Pa) using three different evaporators. The SEM images of the deposited samples within the region “A” indicated in Fig.1 is shown in Fig.2.

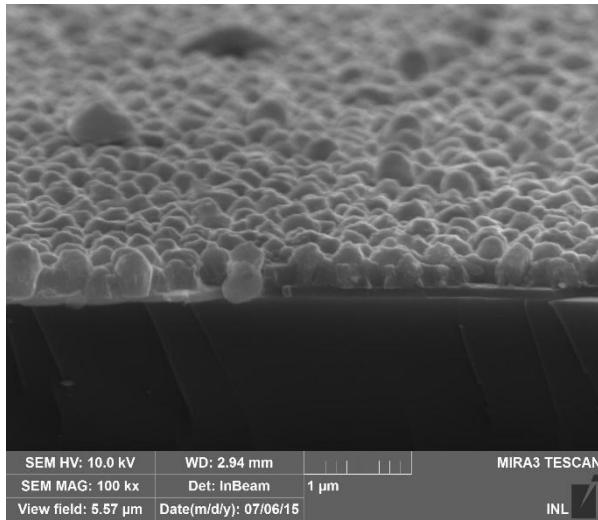
The spherical features with the diameter ranging from 200 through 500 nm in Fig. 2 are typical for Si-Sn alloys [20] and heterostructures [21] obtained using thermal deposition in vacuum. It was shown in the recent works that these features contain metallic (Sn) cores (droplets) and shells of amorphous or combined amorphous/crystalline Si. Such spherical features were shown to form during the deposition of the second (top) layer of amorphous Si. The liquid metal (Sn) droplets are formed during the metal deposition at the substrate temperature higher than the Sn melting temperature of ~ 229 °C. Thermal treatment of such structures at the temperatures higher than the Sn melting temperature initiates α -Si transformation within the shells into a nanocrystalline state. The mechanism of such transformation was discussed in the previous works [21,22]. Due to the features of the surface structure of the sample shown in Fig.2, the light reflection from the surface of the sample is very small. Visually, the surface appears like black soot, featuring thereby significant property of energy loss minimization due to reflection, which is important for the solar cells industry.



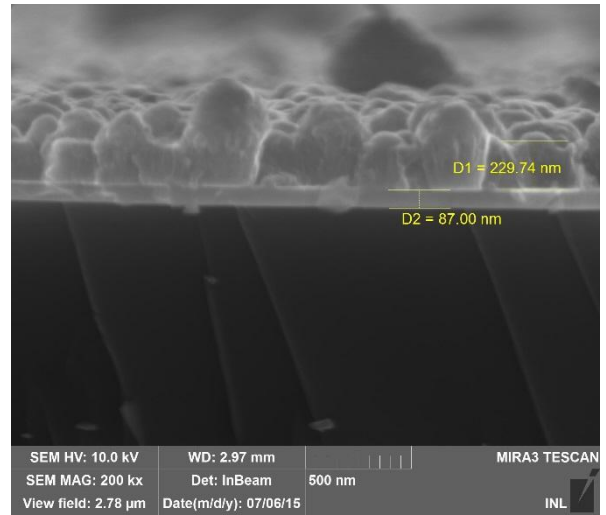
a



b



c



d

Figure 2. SEM images of the 3-layer structure Si/Sn/Si (region “A” in Fig.1). The thicknesses of the deposited layers were X:Y:Z = 100:50:100 nm. Panels a) and b) are images of the surface with different magnification. Panels c) and d) – tilted images of the chipped surface.

As is known, thermal crystallization of amorphous Si occurs at temperatures above 1000 °C . In contrast, MIC – in particular Sn-induced crystallization proceeds at significantly lower temperatures [14,15,21,22], opening new opportunities for the structures like shown in Figs. 1 and 2 through manufacturing of thin films of nanocrystalline Si on flexible and cheap polymer substrates.

The laser annealing is one of possible methods of initialization MIC thin films of amorphous isilicon. This method makes possible to measuring Raman spectra in-situ in the heating process. The analysis of Raman spectra makes it possible to measure the temperature annealing, the size of the formed nanocrystals and their share in the bulk material [23-27].

Both the laser anneal of prepared samples and measurements of Raman spectra were performed using the micro-Raman spectrometer Renishaw. As the lightsource the laser radiation with the wavelength 633 nm and maximum power $P_0 = 10$ mW was used. The laser spot diameter was either 1 μ m or 2 μ m; therefore, the maximum light intensity was $I_0 = 3 \times 10^5$ W cm⁻². Raman spectra were recorded at room temperature in the two regions of the sample (see Fig. 1) – region A (with Sn layer deposited between two α -Si layers) and region B (without Sn layer). Data collection in each experimental run continued for 30 s and three different irradiation intensities were used ($I_1=0.1I_0$; $I_2=0.5I_0$; $I_3=I_0$). The forth experimental run was repeated at irradiation intensity $I_4=0.1I_0$. More Raman runs/scans were applied in some cases as necessary.

Raman spectra of the samples were recorded from the same area of the sample surface and under the same laser intensity several times. This allowed studying the accumulation dynamics of the nanocrystalline phase with irradiation time and, therefore, to estimate the efficiency of laser induced crystallization.

3. Results and Discussion

The Raman spectra recorded from both regions A and B of all samples during the first run with the initial light intensity I_1 exhibited only a wide spectral band with the maximum near 475 cm⁻¹, corresponding to amorphous silicon. During the following experimental runs, the increase of irradiation intensity to I_2 and further to I_3 did not affect the spectra in the B region, but resulted in a narrow peak appearance and rise around 490–500 cm⁻¹ spectral range in the data, collected from the region A (Fig. 3a). This narrow peak was also observed as shifted by Δf_T during the next run at $I_4=I_1$ (Fig.3b). The narrow peak at 490–520 cm⁻¹ corresponds to the nanocrystalline silicon phase [23,24] and the above results evidenced formation of nc-Si as a result of the laser anneal. At the same time, the data collected from the region B of the sample during all experimental runs contained only the features attributed to α -Si (not shown in the figure).

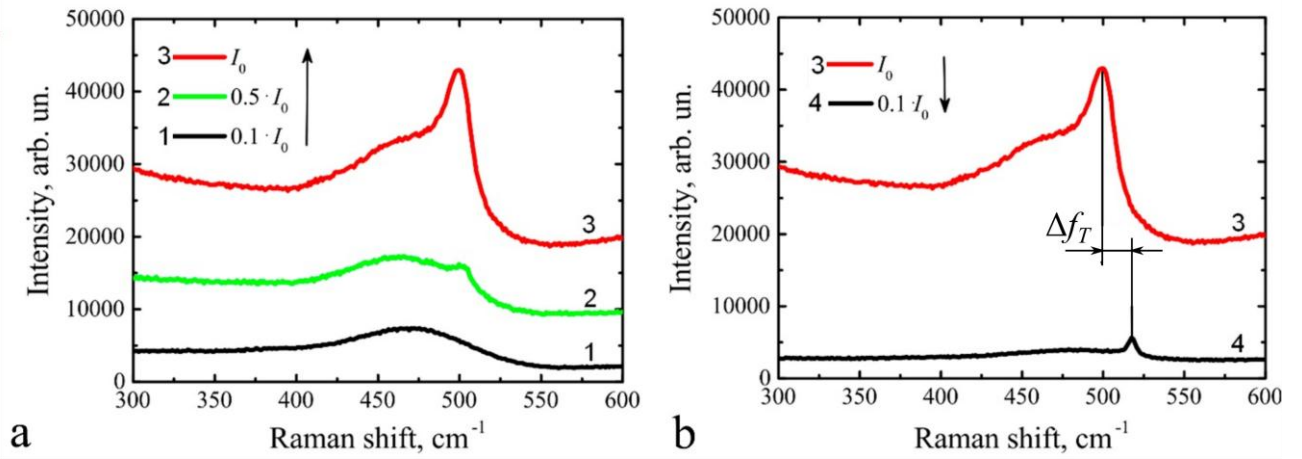


Figure 3. Raman spectra of the sample recorded from the surface in the region A. (a) Irradiation intensity run-to-run increased from $0,1I_0$ to $0,5I_0$ and further to I_0 . (b) Irradiation intensity run-to-run decreased from I_0 to $0,1I_0$. The layers thickness in the sample were X:Y:Z = 100:50:100 nm.

The features of the sample's spectrum evolution with laser anneal presented above were similar to those recorded recently during the thermal anneal of Sn:Si layered structures [20], suggesting that the presence of tin in the investigated layered structure facilitates formation and growth of silicon nanocrystals through the mechanism of metal induced crystallization [21,22].

Note that crystallization of amorphous Si under the influence of laser radiation has been observed by many researchers [28-33]. It is believed that laser-induced crystallization proceeds through local heating of α -Si by laser beam to a temperature above 1000 °C [28-30], or due to the so-called "cold melting" of Si under short but powerful laser pulses (10^{11} - 10^{12} Wcm⁻²) [31-33] – in any case the crystallization is considered to proceed through a thermal mechanism. However, in our case the laser power was not high enough for a thermal crystallization. This is evidenced by the absence of the crystalline Si Raman band for the B region of the samples (outlined in Fig. 1) even after multiple Raman runs/scans at maximum power of the laser radiation.

The crystallites sizes were evaluated from the shift of the crystalline phase peak using a classical phonon confined model [23,24,34]. In addition, the content of nanocrystalline fraction was evaluated from the ratio of the crystalline/amorphous bands areas. The results are summarized in Table 1. The second column of the table shows the thickness of the layers X:Y:Z in nanometers. The third column shows the frequency f of the Raman peak for the crystalline phase at the lowest irradiation power $I_1 = 0,1I_0$ and the increased power $I = kI_0$. The coefficient k values are shown in the 4th column. Note that at the lowest irradiation power I_1 the sample temperature remains close to the room temperature. The 5th and 6th columns present the temperature shift Δf_T of the crystalline phase Raman peak and the estimated maximum local temperature T of the material within the laser spot during experimental runs (scans) [27], respectively (see below for more details on estimation

of these parameters). The number of 30-second runs (scans) for each sample is shown in the 7th column. The shift Δf_R -of the crystalline phase Raman peak position caused by the size-confinement effects at room temperature compared to the peak position of the bulk monocrystalline silicon ($f_R = 520 \text{ cm}^{-1}$) is given in the 8th column. The dominant size R of nanocrystals and the partial volume X_C of the nanocrystalline phase in the sample as estimated using the methods described previously [22,23,34] are presented in columns 9th and 10th, respectively.

Table 1.

1	2	3	4	5	6	7	8	9	10
Sample number	X:Y:Z [nm]	f at $0,1I_0 / kI_0$ [cm ⁻¹]	k	Δf_T [cm ⁻¹]	T [°C]	Number of runs/scans	Δf_R [cm ⁻¹]	R [nm]	X_C [%]
1	50:100:200	508/502	0,5	6	250	5	12	1,9	92
2	100:100:100	516/494	1	22	960	1	4	3,5	90
3	100:100:200	511/500	0,5	11	480	2	9	2,2	92
4	100:200:100	518/499	1	18	830	1	2,5	5,0	86
5	150:100:50	517/497	1	20	870	1	3	4.3	81
6	200:200:200	517/494	1	22	960	5	3	4.3	80

The nanocrystalline phase fraction (partial volume) increased with the laser exposure time. As an example, the dependence of Raman spectra on the exposure time (total time of the runs) is presented in Fig. 4. The data in Fig. 4 were collected during the first (1), second (2), and fifth (5) run (scan) of the spectrum within the same location on the surface. The duration of the each scan was 30 sec.

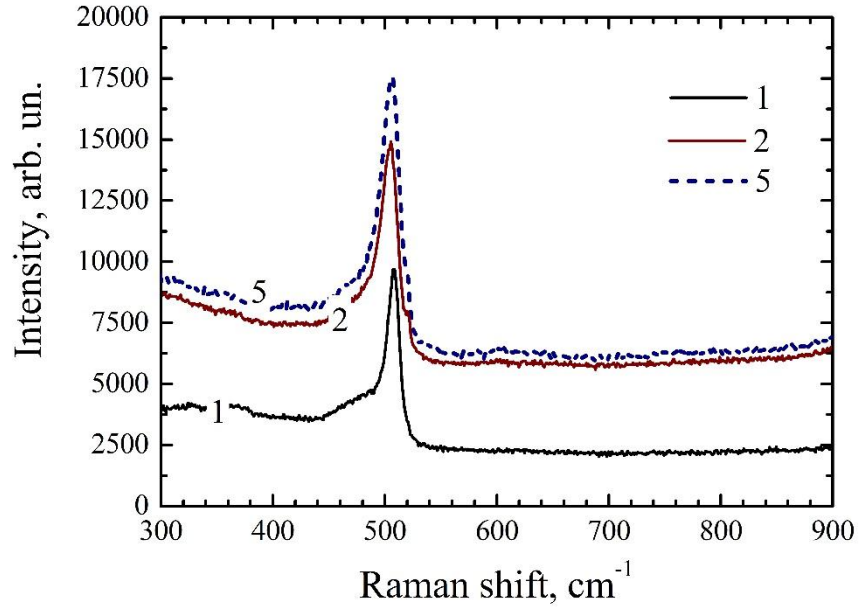


Figure 4. Raman spectra of the sample X:Y:Z = 50: 100: 200 nm at $I = I_0$ recorded during the first (1), second (2), and fifth (5) scan of the same place of the sample.

The increase of the crystalline phase partial volume with irradiation (exposure) time showed saturation. The exposure time at which saturation was observed depended on the initial ratio of the layers thickness (X, Y and Z). The column 10 of Table 1 presents the final value of the nanocrystalline phase partial volume X_c for each sample.

The crystallization of amorphous silicon under laser irradiation is well studied in the literature [28-33]. Several mechanisms of such crystallization were discussed; among them is the mechanism that relies on an excessive heating of α -Si (thermal mechanism). This mechanism takes advantage of high temperature heating of α -Si close to or above the temperature of crystallization ($\sim 1000^\circ\text{C}$). Such heating can be produced with the continuous wave and/or high power pulsed laser radiation.

Let's evaluate the material's temperature within the laser irradiation spot in our experiments. For this purpose, consider the sample that consists of two layers – a top layer Sn/ α -Si composite and a bottom substrate layer. Assume the top composite layer Sn/ α -Si is characterized with the average thermal conductivity K_c and optical absorption coefficient α_c whereas the substrate layer is a glass with the thermal conductivity K_s and absorption coefficient α_s . For simplicity, we neglect the heat absorption in the substrate ($\alpha_s = 0 \text{ cm}^{-1}$). The temperature distribution in this case can be evaluated from the Fourier's-law based thermal conductivity equation

$$\frac{1}{\rho} \frac{\partial}{\partial \rho} \left(K(z) \rho \frac{\partial \theta}{\partial \rho} \right) + \frac{\partial}{\partial z} \left(K(z) \frac{\partial \theta}{\partial z} \right) = -I \cdot g(z) \exp \left(-\frac{2\rho^2}{b^2} \right), \quad (0.1)$$

where ρ and z are the lateral and in-depth coordinates, respectively; $K(z)$ is a spatial dependence of the thermal conductivity:

$$K(z) = \begin{cases} K_c, & z < X + Y + Z \\ K_s, & z > X + Y + Z \end{cases} \quad (0.2)$$

$\theta = T - T_0$ is a laser-induced temperature rise; α is an optical absorption coefficient; b is a beam radius, $g(z)$ is a function describing the heat source distribution in the depth of the sample. In our case $g(z)$ can be written as follows

$$g(z) = \begin{cases} \alpha \exp(-\alpha z) & z < X + Y + Z \\ 0 & z > X + Y + Z \end{cases}. \quad (0.3)$$

The equation (0.1) was written in the cylindrical coordinates, in which the ρ axis was parallel and z axis was perpendicular to the sample's surface. The origin of the coordinate system was chosen in the epicenter of the laser irradiation spot at the sample's surface.

As the boundary conditions, the absence of the heat outflow from the upper surface and the limitation of the solution at the infinity were chosen. In this case

$$\begin{cases} K_c \frac{\partial \theta}{\partial z} \Big|_{z=0} = 0 \\ \theta \Big|_{z, \rho \rightarrow \infty} = 0 \end{cases} \quad (0.4)$$

Additionally, the boundary conditions were supplemented with the discontinuity conditions for the heat flux and temperature at the interface between the composite and glass substrate. In this case, the solution of the equation (0.1) can be presented as follows

$$\theta = \int_0^\infty \theta^H(\lambda z) \cdot J_0(\lambda \rho) \rho d\rho, \quad (0.5)$$

where θ^H is a Hankel transform of the θ ; λ is a positive real number; J_0 is a zero-order Bessel function of the first kind. The value of θ^H was determined from the Hankel transformation of the equation (0.1)

$$\frac{d}{dz} \left(K(z) \frac{d\theta^H}{dz} \right) - \lambda^2 K(z) \theta^H = -I \cdot g(z) \frac{4}{b^2} \exp\left(-2 \frac{\lambda^2}{b^2}\right), \quad (0.6)$$

and the corresponding boundary conditions.

The surface temperature simulation results are presented in Fig. 5a. As one can see from the figure, the temperature even at the epicenter (~ 850 °C) is not high enough to induce processes of the thermal crystallization. Taking in account the absence of the crystalline peak in the B region of the sample, we conclude that silicon nanocrystallites in our experiments were formed as a result of tin induced crystallization of amorphous silicon. As was mentioned above, the temperature required to trigger such crystallization is close to the Sn melting temperature ($T_m \sim 230$ °C). As is obvious from the figure 5a, the regions with the temperature higher than T_m correlate well with the regions of the laser induced surface modification imaged using the optical microscope (see figure 5b).

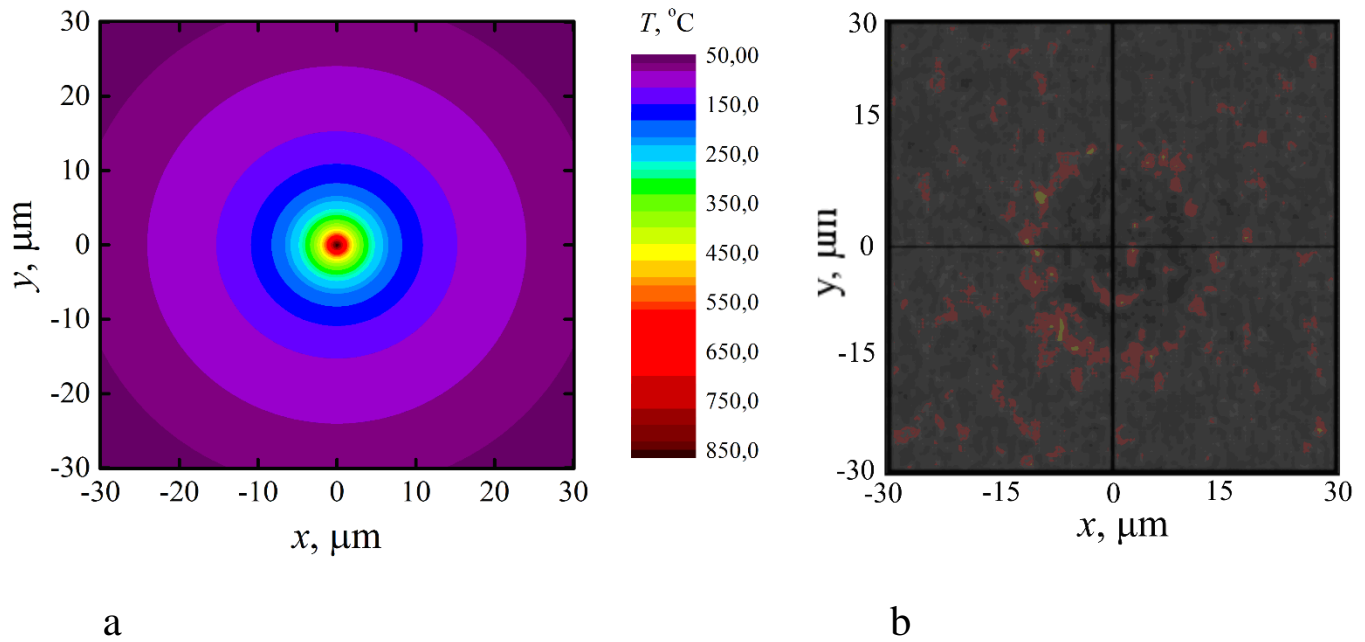


Figure 5. a) Simulation results of the temperature field distribution on the surface of the sample. b) Optical microscope image of the sample surface after 5 scans.

The temperature of the same order of magnitude was estimated from the dependence of the Raman peak shift vs laser intensity. As is known, the position of the Raman peak depends on temperature of the investigated sample. In the crystalline silicon, the Raman peak linearly shifts towards the lower frequency with the increasing temperature. Fig. 6 shows an example of the temperature shift of nc-Si Raman peak observed in our experiments. The data were collected using the sample with the ratio X:Y:Z = 100:200:100 nm. Note different y-axis scales for the two spectra in Fig. 6 as opposed to a single scale in Fig. 3b where the temperature shift was marked as Δf_T .

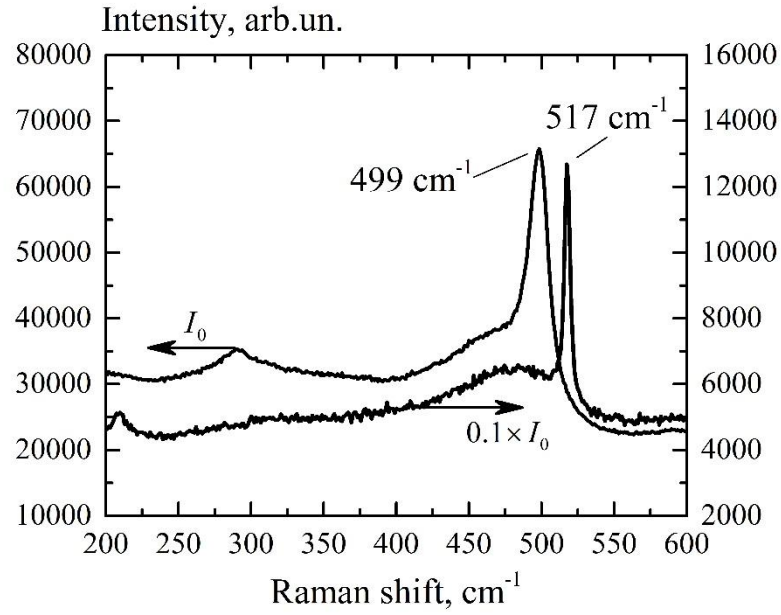


Figure 6. Sample X:Y:Z = 100:200:100 nm. The left axis corresponds to the spectrum recorded using a maximum laser power ($I=I_0$); the right axis corresponds to the spectrum recorded using a minimum power ($I=0,1I_0$)

The Raman peak shifts for different samples are presented in Table 1. The dependence of the Raman peak shift on temperature allowed evaluating the local temperature T in the region of the laser beam heating, also shown in Table 1. As is seen from Table 1, the local temperature in the region of the laser heating was in the range from 350 °C to 960 °C and depended on the ratio X:Y:Z. A relatively large variation in local temperature for different samples can be explained by varying conditions of optical absorption and heat outflow from the laser illuminated zone.

4. Conclusions

Results of this work demonstrated laser-induced crystallization of Sn/(α -Si) layered structures at relatively low temperatures. We suggest that the MIC mechanism described in details recently [21,22] is also valid for the laser-induced crystallization observed in this work. The results showed that Si nanocrystals formation rate, their size and concentration are controlled by the local temperature within the laser spot and duration of the heating process and; therefore, depend on the irradiation power and exposure time to laser radiation. We demonstrated that the in-situ analysis of Raman spectra during laser anneal allows for the in-line control of the crystallites size and partial volume of nc-Si. The number and thickness of Si and Sn layers in the starting material (sample) may be considered as the technological factors that determine the overall thickness of the amorphous-crystalline composite film, distribution of nanocrystals in it, and the amount and status of the residual tin, which is important for the development of new technologies for the solar cell materials.

Acknowledgment

The authors would like to thank Anton Pastushenko from INSA Lyon for providing SEM figures of the samples.

References

1. M.C. Beard, J.M. Luther, and A.J. Nozik, *Nat Nano* **9**, 951 (2014).
2. Z.I. Alferov, V.M. Andreev, and V.D. Rumyantsev, *Semiconductors* **38**, 899 (2004).
3. B. Yan, G. Yue, X. Xu, J. Yang, and S. Guha, *Phys. Status Solidi* **207**, 671 (2010).
4. N.S. Lewis, *Science* **315**, 798 (2007).
5. R. Søndergaard, M. Hösel, D. Angmo, T.T. Larsen-Olsen, and F.C. Krebs, *Mater. Today* **15**, 36 (2012).
6. M. Birkholz, B. Selle, E. Conrad, K. Lips, and W. Fuhs, *J. Appl. Phys.* **88**, 4376 (2000).
7. B. Rech, T. Roschek, J. Müller, S. Wieder, and H. Wagner, *Sol. Energy Mater. Sol. Cells* **66**, 267 (2001).
8. M.K. van Veen, C.H.M. van der Werf, and R.E.I. Schropp, *J. Non. Cryst. Solids* **338-340**, 655 (2004).
9. Y. Mai, S. Klein, R. Carius, H. Stiebig, L. Houben, X. Geng, and F. Finger, *J. Non. Cryst. Solids* **352**, 1859 (2006).
10. H. Li, R.H. Franken, R.L. Stolk, C.H.M. van der Werf, J.K. Rath, and R.E.I. Schropp, *J. Non. Cryst. Solids* **354**, 2087 (2008).
11. R. Amrani, F. Pichot, L. Chahed, and Y. Cuminal, *Cryst. Struct. Theory Appl.* **1**, 57 (2012).
12. G. Fugallo and A. Mattoni, *Phys. Rev. B* **89**, 045301 (2014).
13. O. Nast and A.J. Hartmann, *J. Appl. Phys.* **88**, 716 (2000).
14. M. Jeon, C. Jeong, and K. Kamisako, *Mater. Sci. Technol.* **26**, 875 (2010).
15. M.A. Mohiddon and M.G. Krishna, *J. Mater. Sci.* **47**, 6972 (2012).
16. D. Van Gestel, I. Gordon, and J. Poortmans, *Sol. Energy Mater. Sol. Cells* **119**, 261 (2013).
17. A. Mohiddon and G. Krishna, in *Cryst. - Sci. Technol.*, edited by A. Marcelllo (InTech, 2012), pp. 461–480.
18. V. V Voitovych, V.B. Neimash, N.N. Krasko, A.G. Kolosiuk, V.Y. Povarchuk, R.M. Rudenko, V.A. Makara, R. V Petrunya, V.O. Juhimchuk, and V. V Strelchuk, *Semiconductors* **45**, 1281 (2011).
19. V.B. Neimash, V.M. Poroshin, A.M. Kabaldin, V.O. Yukhymchuk, P.E. Shepelyavyi, V.A. Makara, and S.Y. Larkin, *Ukr. J. Phys.* **58**, 865 (2013).

20. V. Neimash, V. Poroshin, P. Shepeliavyi, V. Yukhymchuk, V. Melnyk, A. Kuzmich, V. Makara, and A.O. Goushcha, *J. Appl. Phys.* **114**, 213104 (2013).
21. V.B. Neimash, A.O. Goushcha, P.E. Shepeliavyi, V.O. Yukhymchuk, V.A. Dan'ko, V.. Melnyk, and A.G. Kuzmich, *Ukr. J. Phys.* **59**, 1168 (2014).
22. V.B. Neimash, A.O. Goushcha, P.Y. Shepeliavy, V.O. Yukhymchuk, V.A.Danko, V.V. Melnyk and A.G. Kuzmich Self-sustained cyclic tin induced crystallization of amorphous silicon. *Journal of Materials Research*, volume 30, issue 20, pp. 3116-3124. (2015)
23. H. Richter, Z.P. Wang, and L. Ley, *Solid State Commun.* **39**, 625 (1981).
24. I.H. Campbell and P.M. Fauchet, *Solid State Commun.* **58**, 739 (1986)
25. M. Balkanski, R.F. Wallis, and E. Haro, *Phys. Rev. B* **28**, 1928 (1983).
26. B. Stoib, S. Filser, N. Petermann, H. Wiggers, M. Stutzmann, and M.S. Brandt, *Appl. Phys. Lett.* **104**, 161907 (2014).
27. S. Périchon, V. Lysenko, B. Remaki, D. Barbier, and B. Champagnon, *J. Appl. Phys.* **86**, 4700 (1999).
28. S. Chen and I.C. Hsleh, *Solid State Technol.* **39**, 113 (1996).
29. A.A.D.T. Adikaari and S.R.P. Silva, *J. Appl. Phys.* **97**, (2005).
30. T.Y. Choi, D.J. Hwang, and C.P. Grigoropoulos, *Opt. Eng.* **42**, 3383 (2003).
31. J.-M. Shieh, Z.-H. Chen, B.-T. Dai, Y.-C. Wang, A. Zaitsev, and C.-L. Pan, *Appl. Phys. Lett.* **85**, 1232 (2004).
32. V.A. Volodin and A.S. Kachko, *Semiconductors* **45**, 265 (2011).
33. A. V Emelyanov, A.G. Kazanskii, P.K. Kashkarov, O.I. Konkov, E.I. Terukov, P.A. Forsh, M. V Khenkin, A. V Kukin, M. Beresna, and P. Kazansky, *Semiconductors* **46**, 749 (2012).
34. E. Bustarret, M.A. Hachicha, and M. Brunel, *Appl. Phys. Lett.* **52**, 1675 (1988).